Narrow band gap cuprous/cupric oxide thin films prepared via sol-gel methods for the electrochemical reduction of CO2

Fabio Vieira, Jean-Bernard Ledeuil, Dominique Foix, Geyla Caridad, Julio Lloret, Laurent Billon, Emilio Palomares, Aurelien Viterisi

Narrow band gap cuprous/cupric oxide thin films prepared *via* sol-gel methods for the electrochemical reduction of CO_2

Fabio Vieira,[a,b] Jean-Bernard Ledeuil,[a] Dominique Foix,[a] Geyla Caridad,[c] Julio Lloret,[c,d] Laurent Billon,[a,b] Emilio Palomares,[a,c,d]* Aurelien Viterisi[a,b]*

A convenient method for preparing cupric and cuprous oxide thin films from a common sol-gel approach is described. The method consists in depositing a thin film of a copper nitrate precursor embedded in a hydroxypropyl cellulose matrix followed by calcination at 500°C. It was found that cupric oxide (CuO) thin films were produced if the calcination step was carried in air, while cuprous oxide (Cu_2O) thin films were predominantly produced if the calcination was carried under a constant-flow rate nitrogen stream. Interestingly, the Cu_2O films were shown to be doped with carbon and nitrogen atoms, with the dopant concentration being related to the nitrogen flow rate used during the calcination step. Importantly, the doping induces a decrease in band gap to lower values than the 2.2eV benchmark for intrinsic Cu_2O. The conductive properties of the doped Cu_2O remained in line with literature values as long as doping was kept minimal. The deposition method of such films is compatible with conductive transparent oxide for application to photo-electroreduction of CO_2.

[a.] *Universite de Pau et Pays de l'Adour, E2S UPPA, CNRS, IPREM UMR 5254*
[b.] *Bio-inspired Materials Group : Functionalities & Self-Assembly, E2S UPPA, Technopole Hélioparc 2 avenue du Président Pierre Angot 64053 PAU CEDEX 09*
[c.] *Institute of chemical research of Catalonia (ICIQ) Avda. Països Catalans, 16 43007 Tarragona*
[d] *ICREA. Passeig Lluís Companys, 28, E-08010. Barcelona. Spain.*

**aurelien.viterisi@univ-pau.fr; epalomares@iciq.es*

†Electronic Supplementary Information (ESI) available: [details of any supplementary information available should be included here]. See DOI: 10.1039/x0xx00000x

Introduction

Greenhouse gas emissions, particularly those of CO_2, are hitting alarming levels. Over the past decades, great efforts have been made by the scientific community to design new catalysts to electrochemically reduce CO_2 into potential feedstock to be reused in a so-called circular economy.[1–7] In this respect, gaseous and liquid C_{2+} products are highly desirable due to the high demand associated with such products and the ease of storage.[8] Among the inorganic catalysts available to efficiently perform the CO2 reduction reaction (CO_2RR) electrochemically, copper has proved to be arguably the best alternative despite the inherent lack of selectivity for one or the other adduct.[9–18] Indeed, the selectivity of copper is tunable to some extent using nanostructured forms of metallic copper[19–23] or copper oxide precursors with a different micro or mesostructure.[24–37,37–39,39–46]. In the latter case, both cuprous and cupric oxide (Cu_2O and CuO) have been employed. Both precursors benefit from bang gaps well-centred in the visible part of the solar spectrum (~2.2 eV and ~1.4 eV) and a strong extinction coefficient. This adds the ability to inject an electron into the LUMO band of CO_2 upon absorption of a photon, the catalyst acting concomitantly as a photocatalyst and an electrocatalyst.[30,36,39,44,46] Recent studies on Cu_2O have demonstrated that the catalytic activity of such precursors is acquired *via* the *in-situ* reduction of the oxide, at least superficially, forming a nanostructured Cu (0) active surface.[37,38,41] The increase in selectivity of such catalysts, compared to bare copper, is attributed to the nanostructure of the Cu (0) active layer acquired from the CuO/Cu_2O precursor and the presence of oxygen vacancies. The case of cupric oxide (CuO) is somewhat similar, and although the direct reduction to Cu (0) from copper (II) is not favoured according to Pourbaix's diagram, local proton concentrations can drive the reduction of CuO to Cu (0) *via* Cu_2O. As a result, the catalytic activity is again predominantly attributed to Cu(0).[32,32] Additional to these mechanistic features, and quite importantly, the catalytic selectivity of the CuO is generally poor unless it is doped or functionalised with different metallic dopants, [24,25,27,30,31,31,33,35,36] or organic dopants.[36]

Based on these early reports, herein we describe the fabrication of cuprous oxide (Cu_2O) and cupric oxide (CuO) thin films using a facile sol-gel method in air or under a controlled atmosphere of nitrogen gas. The method allows for the selective formation of thin films of any of the two types of oxides directly on top of conducting transparent electrodes, such as Indium tin oxide, *via* the deposition of a copper nitrate precursor. The versatility of the sol-gel approach allowed the fabrication of thin films of CuO containing various types of metal dopants. For that matter, metal dopants such as zinc,[25,28] silver or cerium[26,31] were chosen for their demonstrated ability to shift the selectivity of the CO_2RR towards methanol,[30] ethanol, propanol and additional C_{2+} products, respectively.[25,29] Similarly, nitrogen doping was recently shown to strongly shift the selectivity of the CO_2RR towards methanol.[36] With the aim of producing N-doped CuO, we adapted a previously reported procedure from Li *et al.* to our experimental conditions, however it was found that cuprous oxide (Cu_2O) was produced instead. Additionally, the latter Cu_2O, produced from carrying out the calcination step under an N_2 atmosphere, possessed a significantly narrower band gap than that of intrinsic Cu_2O. This was later rationalised by the presence of a high concentration of carbon rather than nitrogen dopants. Furthermore, the CuO and Cu_2O films were characterised by (X-Ray diffraction) XRD, XPS (X-Ray photoelectron spectroscopy) and SEM/Auger emission spectroscopy (AES). Finally, preliminary CO_2 reduction showed some selectivity for forming carbon monoxide (CO) in an aqueous electrolyte at a reasonably low over-potential.

Results and discussion

Background

CuO and Cu_2O thin films are often produced from Cu metal using chemical vapour deposition techniques such as reactive sputtering or physical vapour deposition.[47–49] However, due to the growing interest in copper oxides for applications to the electroreduction of CO_2, new methods have recently been reported. Available work on the production of CuO and Cu_2O catalysts for CO_2 reduction most often involves either the preparation of CuO/Cu_2O nanoparticles *via* hydrothermal or sol-gel methods and their subsequent deposition onto conductive electrodes,[28,30,31,44] the anodisation of Cu sheets to be directly used as electrodes,[35,36] or the electrodeposition from copper precursors.[39,50,51] Nonetheless, CuO and Cu_2O thin films fabricated directly

from sol-gel methods have experienced a recent rise in popularity. Indeed, the ease of fabrication and the ability to produce thick textured films with a high surface area render the latter method very attractive for electrocatalytic applications. Hence several reports on the formation of either CuO or Cu_2O thin films from soluble precursors have appeared recently in the literature. Some used copper chloride (CuCl) as a precursor,[33,52–54] or copper acetate,[55] however, copper nitrate $Cu(NO_3)_2$ seems to have reached consensus as the preferred copper source.[28,31,41,56,57] Indeed, contrary to CuCl, copper nitrate is known to be a very stable source of copper ions, highly soluble in aqueous solutions and organic solvents to some extent. It has been shown to produce CuO crystallites ranging from a few tenths of nanometers to several microns in size, with shapes varying from rods and needles to sheets or flake-like. However, the lower oxidation state of the copper oxide, Cu_2O, is more difficult to synthesise from a sol-gel approach since copper (I) tends to naturally oxidise to its Cu (II) counterpart under the high-temperature oxidative conditions used to produce CuO. The formation of Cu_2O *via* wet deposition techniques has shown to be possible, however, the process is generally carried out in two steps. They involve either the previous formation of Cu (0), which is selectively oxidised to Cu_2O under mild conditions,[45] or *via* the formation of CuO, which is subsequently selectively reduced under specific conditions.[50] Alternatively, Cu_2O has been prepared as thin films by sol-gel methods from a copper (II) precursor in the presence of a reducing agent (e.g. glucose).[58,59] The fabrication of the CuO and Cu_2O films described herein was, therefore, inspired by the above work and based on a copper precursor being calcined at high temperature, typically above 300 °C, in air or under a stream of nitrogen gas to yield either cupric or cuprous oxide selectively.

CuO and Cu_2O film fabrication

Due to the difficulty associated with the fabrication of thick and homogeneous films of CuO using the aforementioned methods, we developed a procedure where copper nitrate ($Cu(NO_3)_2$) is dissolved in DMF containing high molecular weight hydroxypropyl cellulose as an additive. The increase in viscosity provided by the cellulosic derivative allows forming thick and homogeneous films of the copper precursor on glass or ITO substrates, using either blade or spin coating. Moreover, the viscosity can be tuned to suit one or the other technique by simply varying the concentration of the cellulose derivative. Since the copper oxide

described here is to be applied to CO_2 photo-electroreduction, thick films are desirable to maximise catalytic activity. Therefore, blade coating of a concentrated solution of $Cu(NO_3)_2$ and cellulose precursor were used (See SI for details). After deposition of the precursors' layer, the residual DMF is evaporated at 80°C leaving a film of $Cu(NO_3)_2$ embedded in the cellulose matrix, which is readily pyrolysed during a subsequent calcination step (500°C), leaving homogeneous films whose composition is exclusively CuO (see below) when carried out in air. The CuO film is, therefore, conveniently doped with metals by adding know amounts of metal salts to the sol-gel precursor solution, e.g. Zinc acetate (ZnAc), cerium nitrate ($CeNO_3$) or silver nitrate ($AgNO_3$), which will form CuO films with the corresponding metal. Inspiring ourselves by Li and coworkers' work, we assumed that CuO would be readily doped with nitrogen atoms if the calcination was carried out under an N_2 stream. Interestingly, however, it was found that under such conditions, Cu_2O forms instead of CuO. Although surprising at first glance, the formation of the lower oxidation state analogue is rationalised from the lesser availability of O_2 during the calcination and the reducing nature of the cellulose precursor and in the presence of N_2.

Interestingly the absorption properties of the Cu_2O films are significantly changed with respect to literature descriptions of Cu_2O films, displaying a very dark colour even in the case of very thin films (100 nm). N-doping was initially suspected to be responsible for such an apparent decrease in bandgap, however, no nitrogen atoms were detected by XPS (see below). Instead, it was found that, depending on the N_2-stream flow rate, a large quantity of carbon remains embedded in the Cu_2O films as a result of the incomplete pyrolysis of the hydroxypropyl cellulose matrix. The thorough analysis of these films is expounded below, showing that the composition of the films is consistent with the presence of an amorphous form of elemental carbon, as observed in a recent report on carbon-supported CuO electrodes.[55] Interestingly, the amount of residual carbon in the Cu_2O films highly depended on the flow rate used during the high-temperature calcination step (see below).

X-ray diffraction characterisation

The structural characterisation of the produced CuO and Cu_2O films was first carried out by X-Ray diffraction (XRD) on a benchtop diffractometer.

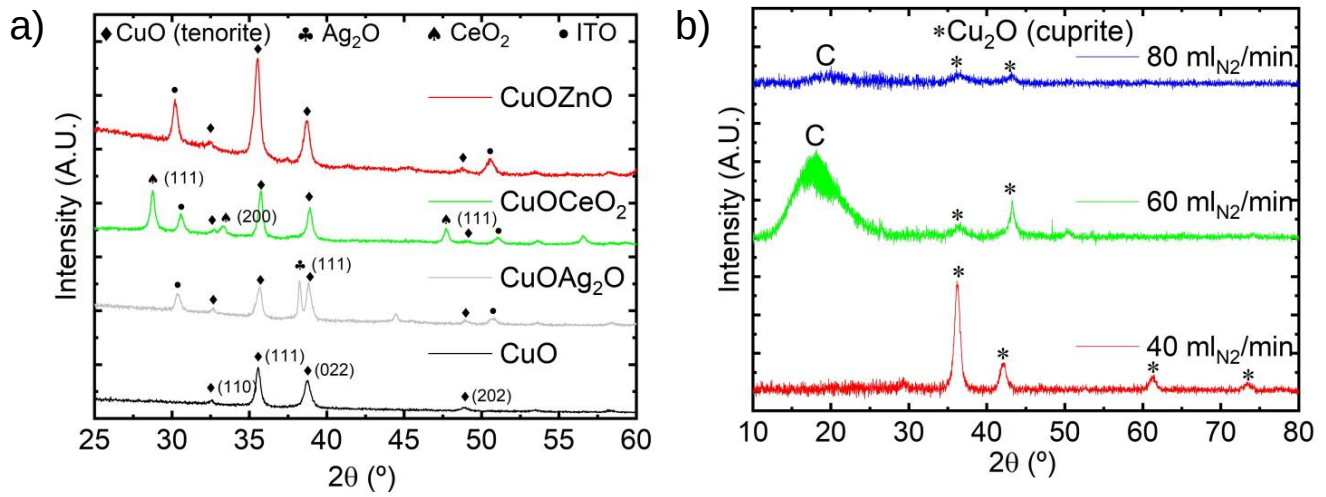

Figure 1a shows the XRD diffractograms of all doped and un-doped samples whose fabrication procedure implied a calcination step in air. The characteristic diffraction pattern of the monoclinic tenorite CuO crystalline phase confirms the presence of an exclusive CuO fraction in the bulk of the films.

However, diffractograms of films calcined in N_2 displayed the characteristic cubic cuprite Cu_2O crystalline phase (

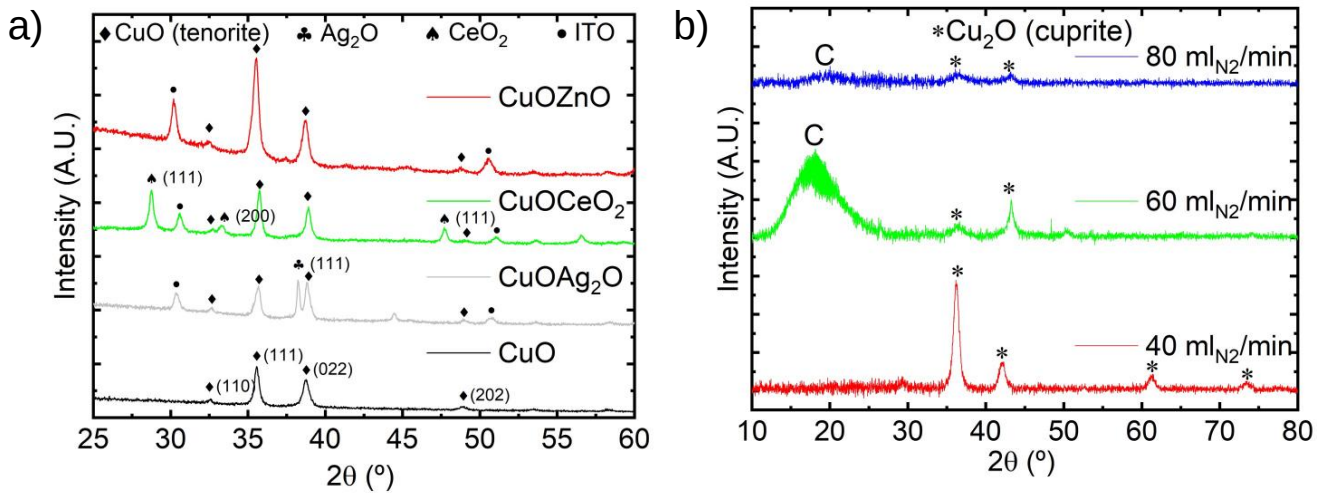

Figure 1. a) stacked diffractograms of doped and undoped CuO thin films deposited on glass slides; b) stacked diffractograms of Cu_2O thin films deposited on glass slides. The background was corrected against a diffractogram of a blank glass substrate to subtract the typical amorphous broad diffraction peak of the glass.

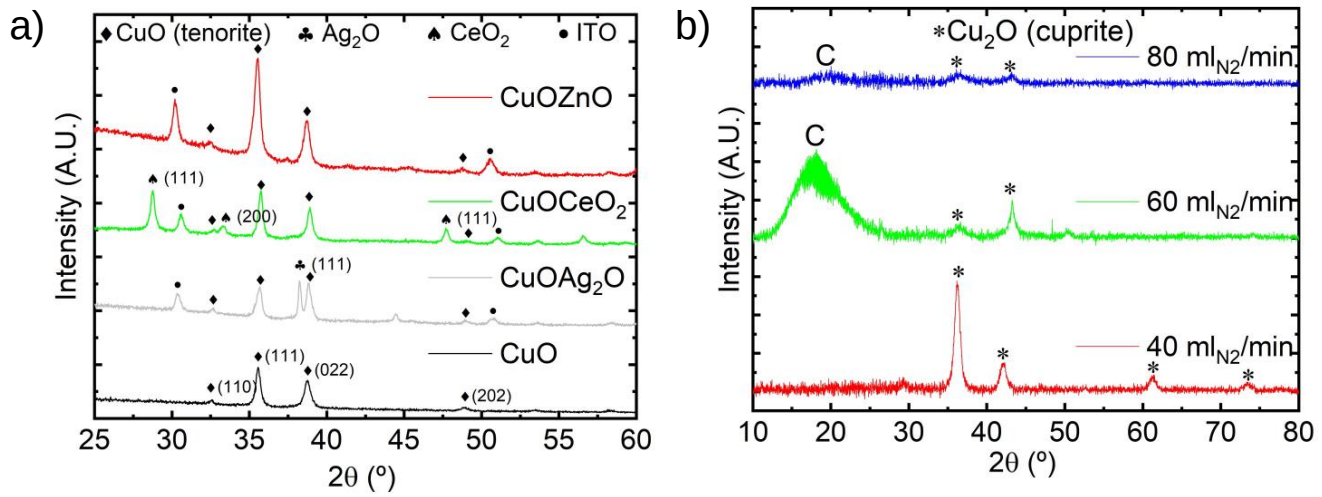

Figure 1b). The crystallite sizes calculated using the Scherrer method range from 10 nm to 20 nm for both types of oxides (

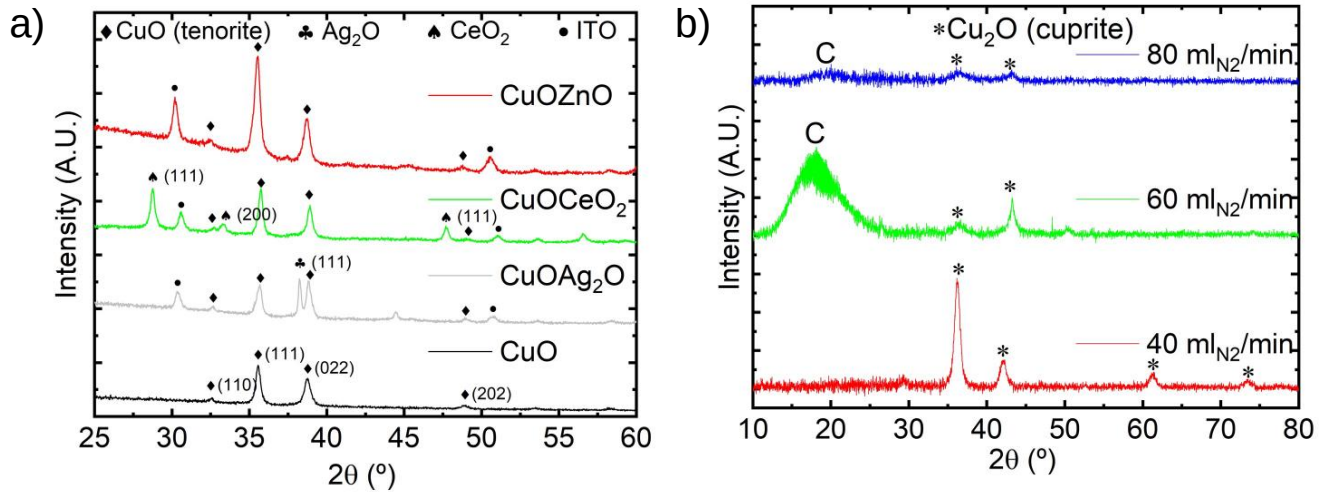

Figure 1). The latter parameter was calculated using the Bruker XRD processing software, *Diffrac Plus*, after the background was corrected using the diffractogram of a blank substrate identical to those on which the copper oxides were deposited.

The size of the crystallites is relatively modest; however, it is consistent with typical values reported for CuO and Cu_2O thin films. Importantly, the diffractograms do not show detectable amounts of crystalline adducts of metallic copper (Cu(0)). Additionally, the metallic dopants are crystalline enough to be detected as their respective oxides in the case of cerium and silver. However, no crystalline fraction of ZnO was detected on the corresponding Zn-doped CuO films' diffractogram. In the latter case, the metal dopant is not seen to

incorporate into the CuO phase to a significant extent either, as seen by the diffractogram corresponding to pristine CuO. The Cu_2O samples follow a similar trend in that their diffractograms do not show any significant difference from the expected Cu_2O cuprite phases (

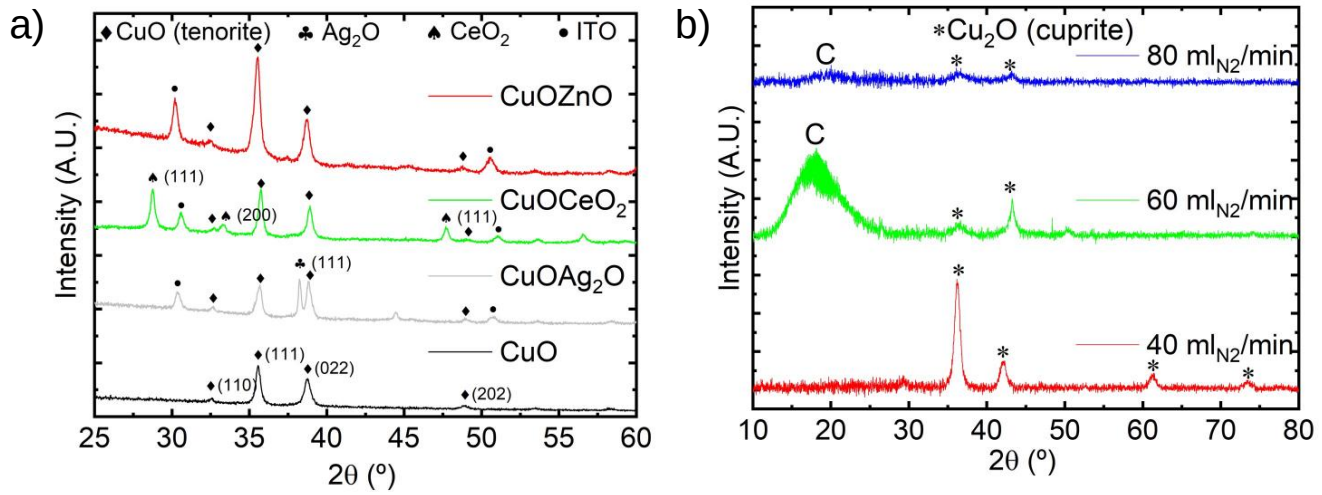

Figure 1b). Interestingly, the diffractograms of the Cu_2O films calcined at different N_2-flow rates show somewhat different crystalline features with respect to one another. As seen in

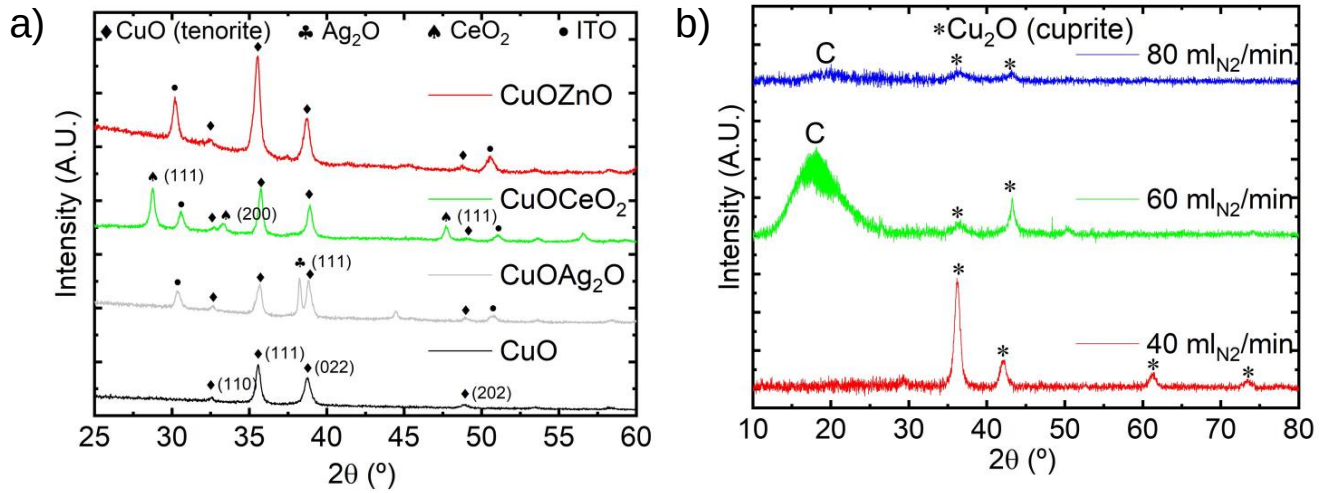

Figure 1b, their respective crystalline volume varies significantly with increasing N_2 flow rate. Importantly, a very broad peak of semi-amorphous material at $2\theta = 17°$, attributed to elemental carbon, is apparent from the samples calcined at a 60 mL/min and 80 mL/min N_2-flow rate. The peak assignment was made *a priori* based on earlier reports,[55] nevertheless, it was later unambiguously confirmed by XPS and SEM/AES characterisation (see below). The amount of carbon is seen to be particularly elevated in films processed at medium N_2-flow rates (60 mL/min), as evidenced by the intensity of the peak. Interestingly, the intensity of

the corresponding peak is much lower in samples calcined at 80 mL/min and non-existent in samples calcined at a low flow rate (40 mL/min). Moreover, a concomitant decrease in overall crystalline volume from both the Cu_2O fraction and carbon fraction is observed upon increasing the N_2 flow rate up to a point where the film calcined under an N_2-flow rate above 60 mL/min can virtually be considered amorphous. The presence of carbon is readily rationalised by the fact that the final pyrolysis step in the formation of the oxide is carried out under a controlled inert atmosphere where O_2 is not present in other than trace amounts in the reaction chamber. Indeed, under such oxygen-depleted conditions, the carbon-based matrix (hydroxypropyl cellulose) is not expected to fully oxidise to CO_2 as for the CuO films. Thus, the carbon backbone of the former cellulose additive remains embedded in the metallic oxide films as elemental carbon.

Scanning electron microscopy/ Auger emission spectroscopy (SEM/AES)

To assess the impact of the dopants on the films' surface morphology, we carried out low-resolution SEM imaging (**Erreur ! Source du renvoi introuvable.**). Although unexpected from the crystalline properties of

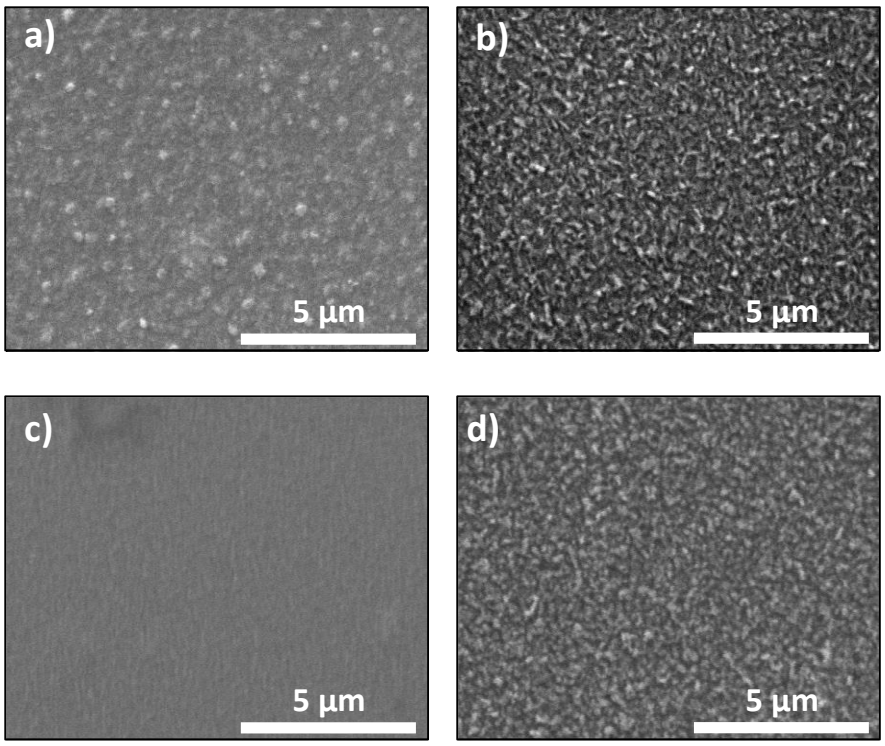

Figure 2. Low resolution scanning electron micrographs of cupric oxide films a) undoped; b) doped with cerium c) doped with zinc d) doped with silver.

the films, i.e., small crystallite sizes, most of the copper oxide films studied herein showed a relatively high degree of roughness with peak-to-peak values averaging microns in some cases. This trend is in line with previous work on copper oxide thin films prepared *via* sol-gel methods. However, in our case, the surface's roughness shows to be dependent on the nature of the element with which the film is doped. Indeed Zn-doped samples are seen as texture-less on an average SEM magnification, while the texture gradually increases when moving to undoped, Ag-doped, to Ce-doped (**Erreur ! Source du renvoi introuvable.**).

To further investigate the composition of the bulk of the film, we carried out SEM-AES imaging on the Cu_2O films, where ion etching with argon plasma was used to penetrate through the film's depth. High-resolution SEM micrographs and their corresponding Auger spectra are shown in Figure 3. The surface morphology of the films calcined at 60 and 80 mL/min N_2 flow rate shows an increase in roughness with increasing flow rate. Indeed, SEM micrographs of Figure 3a, 3b and 3c show a net increase in protrusion density per unit area, reaching a somewhat overwhelming roughness in the case of films calcined at 80 mL/min, with particle sizes approaching microns in size. Interestingly, this increase is not linked to an increase in crystallinity—quite the contrary since the crystalline volume is seen to decrease with increasing flow rate. Therefore, the increase in roughness is likely linked to an increase in the kinetics of oxide formation, inducing fast precipitation of largely amorphous Cu_2O particles. Interestingly, these textured surfaces are reminiscent of previously reported work on copper oxide films made *via* sol-gel methods.[37,50]

Importantly, the Auger spectra confirm that elemental carbon is present in significant amounts throughout the bulk of the films and that its distribution is rather homogeneous across the thickness of the layer. Indeed, after an initial low energy ion etching event for removal of adventitious carbon and oxygen species (usually present on the surface of most air-exposed samples), the relative distribution of the main elements, i.e., C, Cu, O, remains nearly identical in each sample, even after several ion etching events (Figure S9). The distribution of carbon through the bulk of the samples shows a very similar trend to the results obtained from XRD. A large amount of carbon remains in the bulk when the films are calcined under a higher flow rate (60 and 80 mL/min), while carbon is present in much lower amounts in the samples calcined at 40 mL/min.

Noteworthy, the latter films show the incorporation of significant amounts of nitrogen atoms in addition to carbon atoms. This can be rationalised by the presence of a large excess of N_2 during the Cu_2O formation,

which likely intercalates as a dopant in the Cu_2O structure, as seen in other methods of Cu_2O formation (Figure 3g).[36,60] SEM images show, however, that the surface of the films fabricated under a 40 mL/min N_2 flow rate is rather inhomogeneous, with protrusions in the range of a few tens of nanometers in diameter scattered along the surface. A semi-quantitative composition analysis based on experimental spectra peak deconvolution using external references (Cu, CuO and Cu_2O) was carried out (see SI). Data confirms that the latter films are mostly composed of pure Cu_2O species, with CuO present only in trace amounts. Additionally, it shows that the concentration of copper is higher with respect to the carbon atoms within the protrusions (Figure S10).

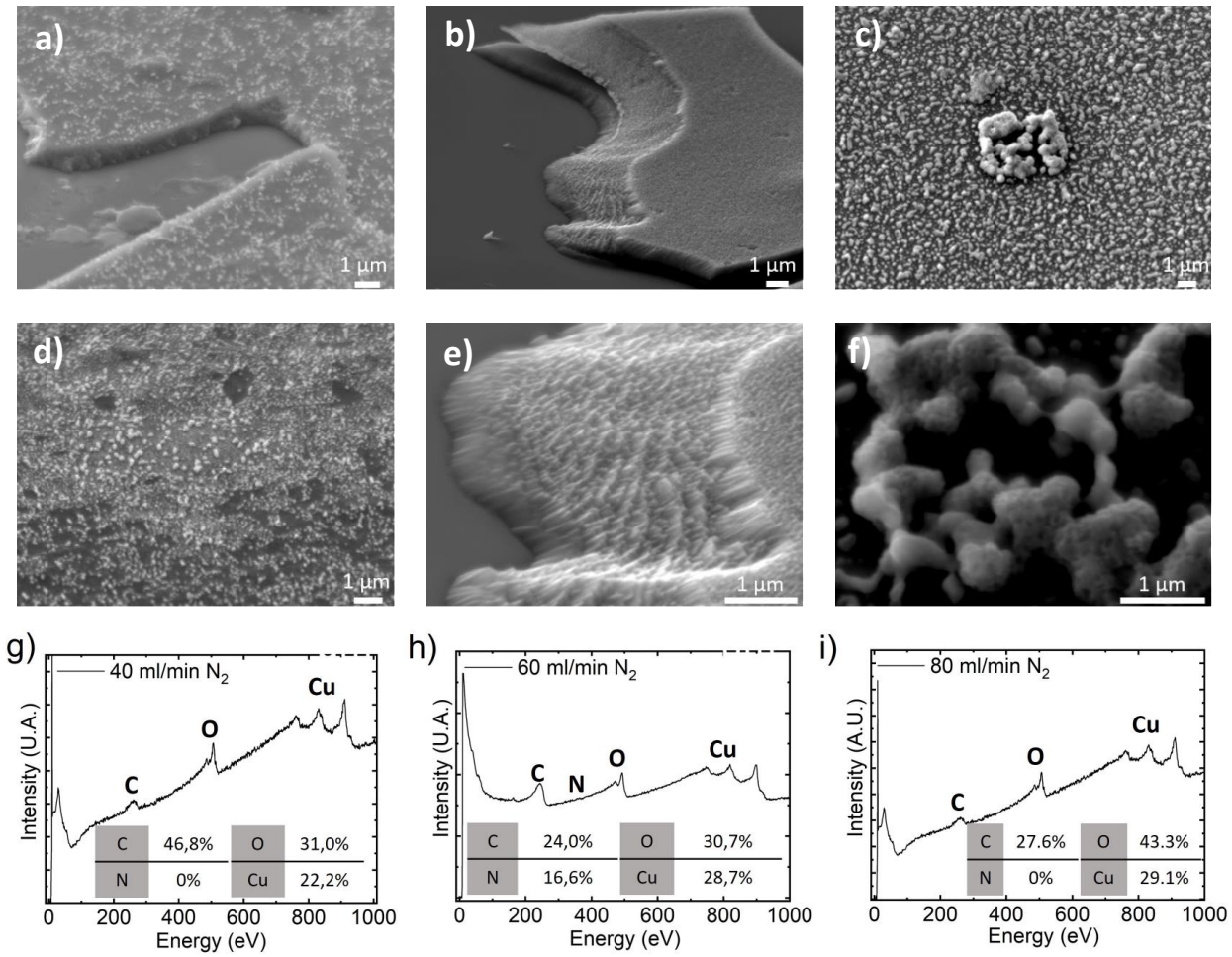

Figure 3. High resolution SEM imaging of thin films of Cu2O calcined at different N_2 flow rates a) and d) 40 mL/min; b) and e) 60 mL/min; c) and f) 80 mL/min. Auger spectra recorded from thin films of N_2-annealed cuprous oxide thin films at the following flowrates g) 40 mL/min h) 60 mL/min i) 80 mL/min.

The latter methodology was applied to the films made at a higher flow rate, showing that the copper fraction remains predominantly of cuprous oxide (Cu_2O) nature, however, a substantial amount of CuO is accounted for (Figures S11 to S14). Although counter-intuitive at first glance, greater amounts of CuO in higher-

flowrate samples can be rationalised by the availability of oxygen atoms from the hydroxypropyl cellulose organic matrix. The pyrolysis of the latter oxygen-rich molecule is found to be incomplete with an increasing N_2 flow rate, leaving an excess of oxygen atoms to be included in the copper oxide structure. Concomitant to the increase in CuO relative to Cu_2O, a stark increase in carbon content is also observed. This is particularly the case for samples calcined at 60 mL/min, where carbon is now the dominant element in the film, confirming the data from XRD. A similar rationale for the presence of CuO can be applied in this case, whereby the high carbon content underpins the evidence of incomplete combustion of the cellulosic matrix under a higher N_2 flow rate. As this fraction of CuO is not detected by XRD and is only present in significant amounts in the 60 and 80mL/min films, i.e., containing a larger amount of carbon, it can be assumed that this species is embedded in the carbon matrix in an amorphous state.

X-Ray photoelectron spectroscopy

To shine light on the nature of the films' surface, XPS characterisation was utilised. The XPS spectra complement the analysis from the SEM-AES characterisation, although limiting the analysis to the very few top atomic layers of the film. This comes with a significant drawback in that native surface oxidation, which is readily expected for such types of copper oxide materials, renders the composition ratio between the two types of oxides unrepresentative of the bulk of the materials. However, XPS provides accurate quantification of the absolute elemental composition of the films. As such, the satellite Auger bands characteristic of both Cu (II) et Cu (I) species are present in all the samples of either CuO or Cu_2O. Furthermore, no electron emission from Cu (0) is detected either, confirming that the surface of the catalyst is composed solely of Cu(II) and Cu(I) species (Figure 4a). In the case of the sample calcined at 60mL/min, no characteristic peak of CuO was detected, however the peak characteristic of copper hydroxide ($Cu(OH)_2$) is present. The presence of $Cu(OH)_2$ presumably stems from the reaction of CuO with surface-bound water molecules. Indeed, CuO is known to readily dissolve in mild acidic aqueous conditions, forming the corresponding Cu (II) salt. For the sample calcined at 80mL/min, CuO is the only species detected, in contrast with SEM-AES results, which show a majority of Cu_2O in the bulk of the film. This indicates that partial pyrolysis of the

hydroxypropyl cellulose matrix provides the Cu_2O film with enough oxygen to form a very thin layer of pure

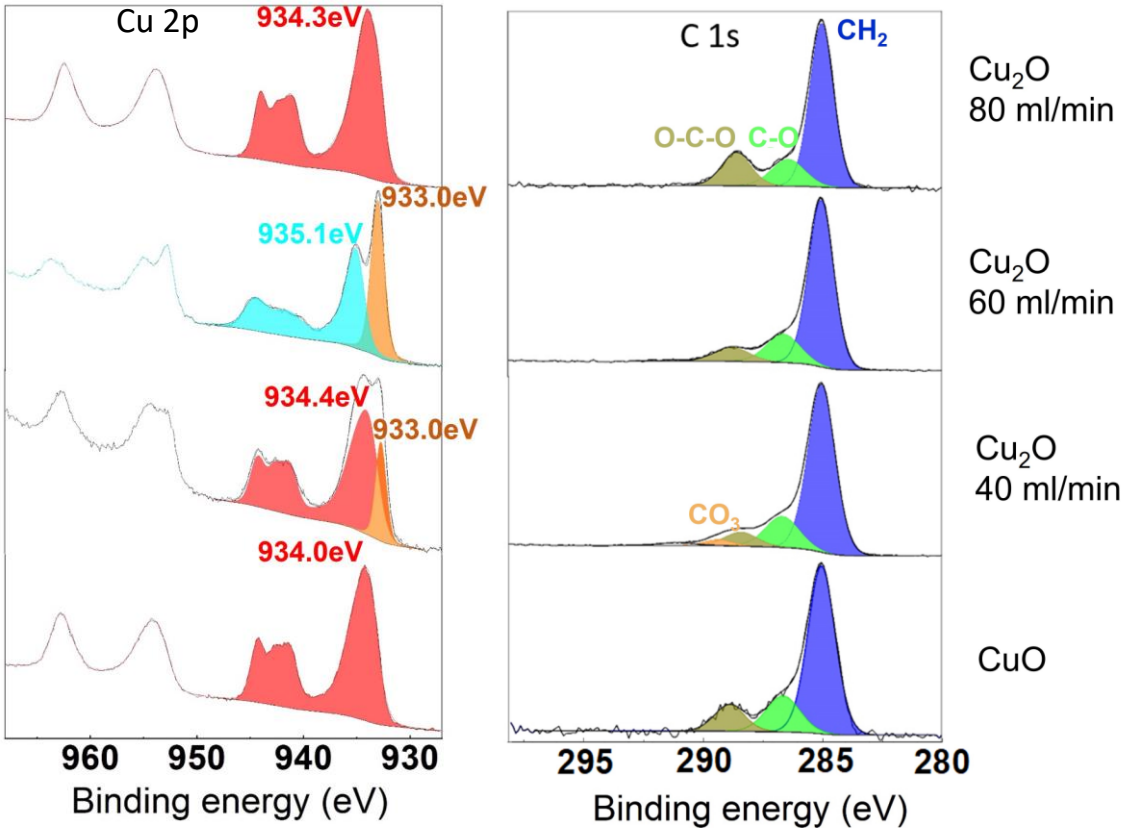

Figure 4. XPS spectra of CuO and Cu2O thin films a) showing the Cu and Cu 2+ Auger satellites emission peaks; b) showing the C-O and C=O emission peaks.

CuO on the surface of the film.

Table 1 summarises the relative composition of the elements in all the films characterised, confirming that a large amount of carbon is present in both oxides, corroborating the data from XRD and SEM-AES. Additionally, emission peaks with binding energy corresponding to characteristic C-O and C=O bonds are also detected in the XPS spectra, evidence of incomplete pyrolysis of the cellulose matrix. Figure 6b shows the characteristic emission peaks of the *C1s* electrons with their characteristic C-O and C=O signature. These adducts likely account for a significant fraction of the total elements, as seen by the mismatch between Cu and O elements in the fractional composition analysis (Table 1). The mismatch is more predominant for the films of Cu_2O calcined under high N_2 flow rates (e.g. Table 1, line 3), where the amount of oxygen is over 6-fold higher than that of Cu. Overall, these values are consistent with the trend observed by XRD. That is, Cu_2O films calcined under a high N_2 flow rate are seen to contain a large proportion of carbon with respect to the copper and oxygen content, while those calcined at 40 mL/min have a lesser amount of carbon

compared to copper and oxygen. The ratio of Cu to C in the latter case is in a similar range to that of CuO films (Table 1).

Table 1. Elements molar fraction of CuO and Cu_2O films determined by XPS

	C	O	Cu	N
CuO	7.4	49	35	
Cu_2O (40ml/min)	21	41	31	
Cu_2O (60 mL/min)	66	22	3.4	2.2
Cu_2O (80ml/min)	53	29	5.4	2.3

UV-Vis and conductivity characterisation

Stark similarities in light absorption properties of the cuprous and cupric oxide films prompted us to carry out an in-depth characterisation of their absorption and electrical properties. That is, both types of oxides show a dark brown to black colouring. Although this is expected for CuO, regular Cu_2O was expected to have an absorption onset well shifted towards higher energy wavelengths, usually appearing reddish when deposited as thin films as a result of a significantly wider band gap than that of CuO (2.2ev *vs* 1.4eV, respectively). To verify that the light absorption properties of the Cu_2O films were linked to a significant decrease in band gap, the absorption spectra of the films were recorded in the UV-visible range, and the effective band gap was calculated *via* a Tauc plot (Figures S15 to S18). The absorption spectra and Tauc plots for the two types of oxides are shown in

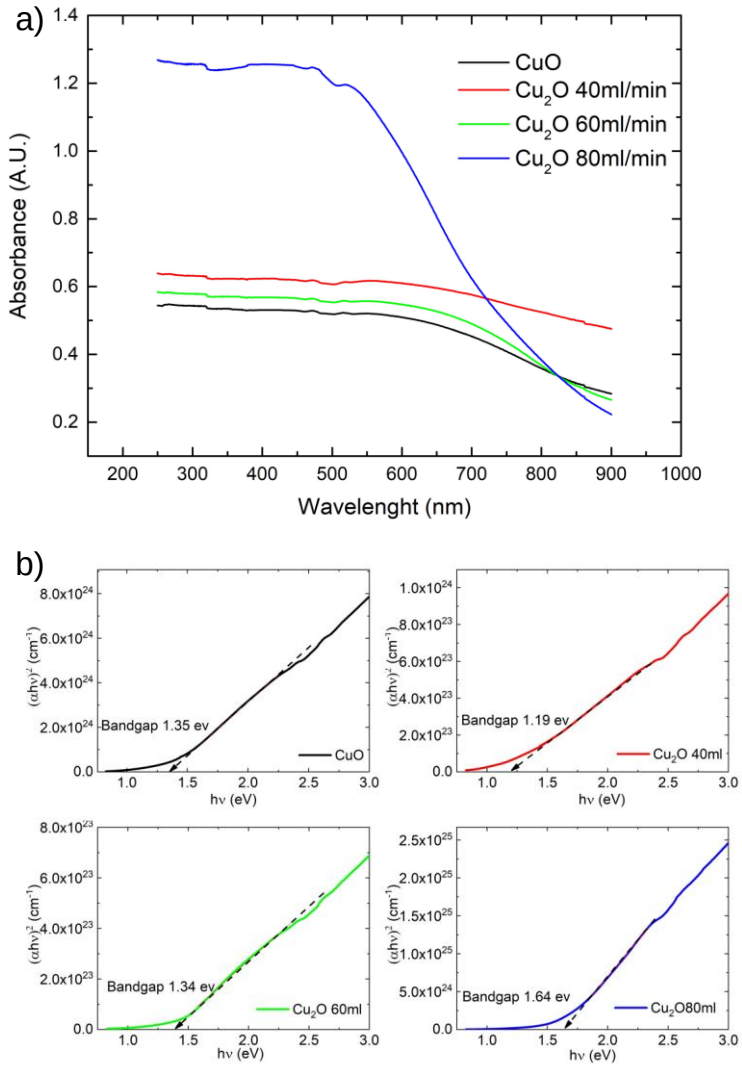

Figure 5. The UV-Vis spectra confirm the visual similarity between the two types of oxides, and the Tauc plot further confirms that the Cu_2O underwent a very significant decrease in band gap (Table 2). Although doped Cu_2O layers with wider or narrower band gap than intrinsic Cu_2O have been described in the literature, such a stark decrease is quite unique for Cu_2O. The rationale behind this apparent decrease is likely the result of heavy carbon and nitrogen doping.

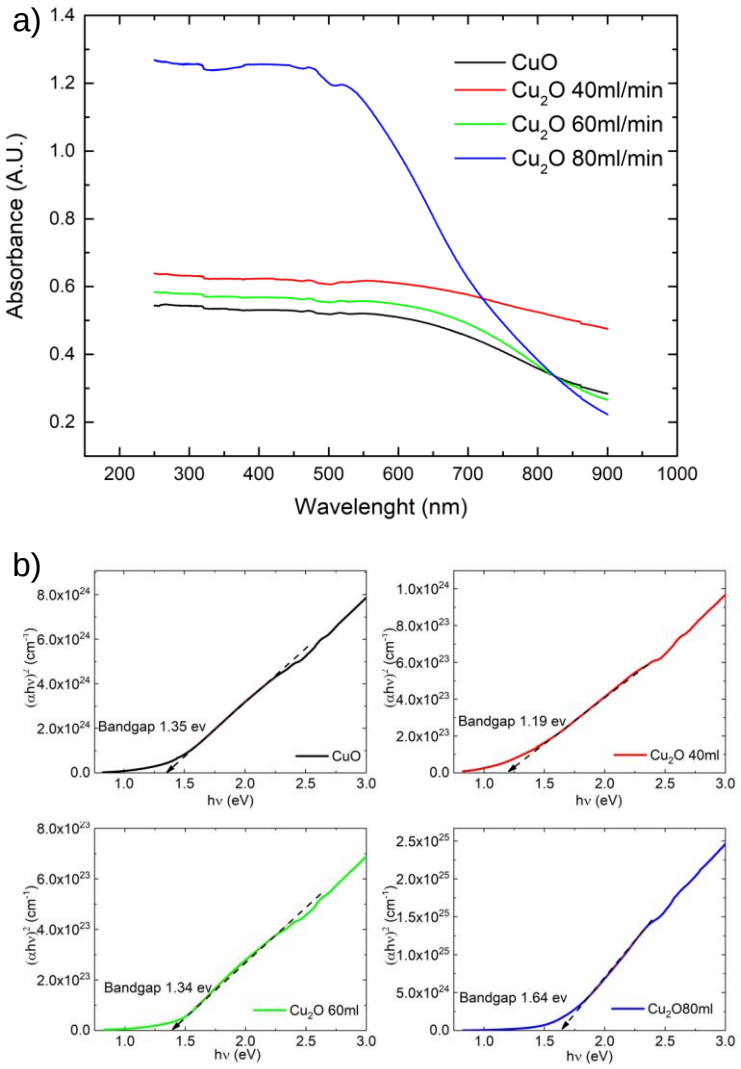

Figure 5. (a) Absorbance spectra and (b) Tauc plot of the CuO and Cu_2O films deposited on quartz substrates.

Due to the potential applications in photogeneration devices (e.g., photovoltaics) of such a narrow band gap Cu_2O, it is essential to assess the impact of the doping concentration on the electrical conductivity of the films. For that purpose, a home-built Van der Paw apparatus was used to measure surface conductivity with a four probes setup. As expected, the heavily doped Cu_2O (60 and 80 mL/min N_2-flow rate) showed a conductivity value about two orders of magnitude lower than its more lightly doped analogue (40 mL/min N_2-flow rate). Nevertheless, the conductivity is comparable to available values from the literature for solution-processed Cu_2O (table 2).[61–63] The conductivity reaches 2.28 S/cm for samples calcined at 40 mL/in,

which is remarkable since it stands in the same range as CuO films. Overall, this data shows that carbon doping has a strong impact on the band gap of Cu_2O, as well as on the electrical conductivity. However, a compromise between dopant concentration and reasonably high electrical conductivity can be found, as exemplified by the samples calcined at a 40 mL/min flow rate.

Table 2. Bandgap, conductivity and ratio between Cu(I) and Cu(II) for each of the copper oxide films.

	Conductivity (S/m)	Optical band gap (eV)	Cu (I)/Cu (II) relative ratio (%)
CuO	6.25	1.35	41/59
Cu_2O (40ml/min)	2.28	1.19	97/3
Cu_2O (60 mL/min)	0.026	1.34	33/67
Cu_2O (80ml/min)	0.015]	1.64	63/37

Electrochemical reduction of CO_2

The ability of the different copper oxides to catalyse the CO_2 reduction reaction was assessed. To do so, the films were deposited on indium tin oxide (ITO) substrates in identical conditions as above. The choice of ITO for that purpose was motivated by the future goal of applying our films to the photo-electroreduction of CO_2, hence the necessity of a transparent and conductive substrate. Therefore, ITO substrates of a nominal 15 ohm/sq sheet resistance were used for this purpose. A preliminary study was carried out to verify that the temperature used during the calcination step had no detrimental effect on the conductivity of the substrate. A significant drop in sheet resistance was observed upon calcination at 500 °C. Nonetheless, the final sheet resistance remained sufficiently low for electrochemical experiments, with a value reaching about 159 ohms/sq (Table S2). Additional to the electrical properties of the substrates, a linear sweep voltammetry (LSV) towards negative potentials in a three electrodes cell set up in the conditions used for the CO_2RR allowed establishing the experimental range under which ITO substrates are stable during the electrochemical experiment. Voltammograms indicate that reduction voltages up to about -0.90V (*vs* RHE) could be used. However more negative potentials have a direct impact on the integrity of the ITO layer, which is seen to reduce to In (0) or Sn (0) species, as evidenced by the resulting metallic lustre (Figure S1).

A subsequent LSV experiment with an ITO substrate on top of which a CuO layer was deposited confirmed that the ITO layer is compatible with CuO as a catalyst in that the onset of reduction in a $KHCO_3$ (0.5M) solution is significantly lower than the reduction potential of ITO. Indeed, Figures S2 to S5 show the LSV of undoped CuO and Cu_2O in N_2-degassed and CO_2-saturated electrolytes. A faradic current at voltages as low as -0.40V (*vs* RHE) was observed in both cases. Additionally, the latter experiment indicates an explicit reducing catalytic activity, presumably towards H_2O or CO_2, which are the predominant species in solution. Therefore, the subsequent quantification of the electrocatalytic activity of the copper oxide layers towards the CO_2RR was carried at reduction potentials ranging from -1.0 to -0.60V *vs* RHE in $KHCO_3$.

With these preliminary parameters established, we then carried out constant potential chronoamperometry experiments to evaluate the rate at which the catalysis reaction occurs. Experiments at 0.60V *vs* RHE show a low reaction rate, with current densities around 1 mA/cm^2, while the main product of catalysis is H_2. The rate increases significantly, however, under more negative electrical potentials, with currents reaching values of 2.2 mA/cm^2. However, the copper oxide films showed a strong tendency to delaminate in the very early stages of the catalytic process under electrolysis at potentials below -0.50V *vs* RHE. This effect is evidenced by the stark decrease in current density recorded in all chronoamperometry experiments, as seen in Figure 6 (black curve). This effect is likely the result of water molecules diffusing through the copper oxide layer and being subsequently reduced to H_2 at the ITO/copper oxide interface. The production of gas at the interface

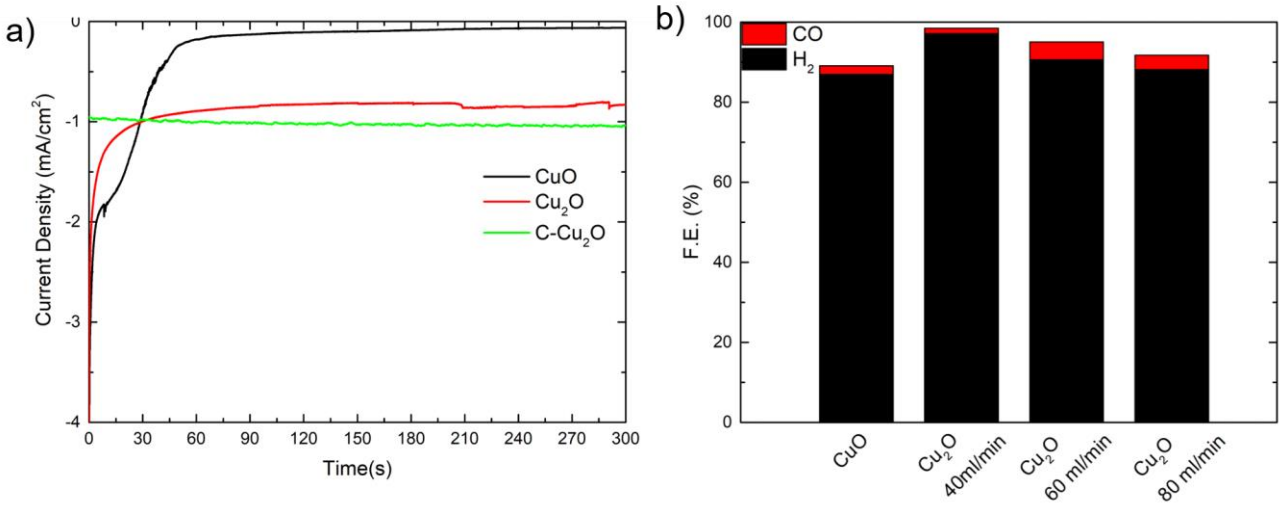

Figure 6. a) Chronoamperograms of CO_2 reduction experiments carried out with the three types of copper oxide films at -0.6 V (*vsRHE*) for 5 minutes; b) Faradic efficiencies of the corresponding experiments calculated from the quantification of the electrochemical cell head space and from the expected quantity of produced from the electrical charge passed through the catalyst during the experiment.

would therefore be the reason for the film delaminating. Additionally, the structural modification of the catalyst surface under electrolytic conditions is expected to significantly weaken the binding interaction between the film and the ITO surface (Van der Waals or electrostatic). Further evidence for the process to be electrochemically triggered is that no delamination occurs in a similar time frame when the film is left in the electrolyte with no electrical potential applied. To circumvent this setback, a thin layer of TiO_2 was intercalated between the ITO and CuO (Figure S7), however, with no significant improvement. Nonetheless, the electroreduction reaction was quantified *via* head-space gas chromatography and the total faradic efficiency was calculated. Figure 6b shows the faradic efficiency and the product distribution for the three main catalyst types studied herein for chronoamperometry experiments carried out at -0.60V (*vs* RHE) for the longest time before delamination occurred. As seen in Figure 6a, delamination occurred within seconds of the process's initiation in the case of CuO, as evidenced by the fast current drop. Cuprous oxide films proved more robust, with delamination occurring later than 300 seconds after the electrolysis had begun. Despite these limitations, quantification after a short electrolysis time showed a nearly quantitative total faradic efficiency for all catalyst types. However, the selectivity of the CO_2RR is overwhelmingly shifted towards H_2, although a modest quantity of CO could be detected.

Conclusion

To conclude, we have developed a convenient sol-gel method to prepare both cupric and cuprous oxide from a single precursor by controlling the gaseous atmosphere of the pyrolysis step. That is, carrying out the pyrolysis step under a saturated atmosphere of N_2 has a reducing effect on the copper precursor, forming Cu_2O exclusively. We additionally demonstrated that under the latter conditions, the Cu_2O is doped with significant amounts of carbon resulting from the incomplete pyrolysis of the cellulosic additive used during the film deposition. The extent of doping has been shown to be linked to the N_2 flow rate used in the pyrolysis step. Nitrogen is also seen to dope the Cu_2O film when a low N_2 flow rate is used, presumably from nitrogen atoms coming from the nitrate precursor counter ion. Importantly, carbon doping has a significant impact on the band gap of the Cu_2O films, decreasing it from a standard experimental value above 2 eV to a value in

the same range as that of CuO (1.3 eV). This is a unique feature which is expected to have an impact on the photocatalytic properties of these films. The electrical properties of the films were characterised, showing a decrease in conductivity with increasing carbon doping concentration. However, the conductivity of lightly C-doped Cu_2O was only slightly lower than that of CuO. Early electrochemical catalytic activity towards CO_2 reduction was characterised by chronoamperometry and quantification of the gaseous products. Results showed very similar activity for all three copper oxide types studied, showing modest carbon monoxide (CO) faradic efficiencies. The latter study was somewhat hampered by the fact that the films showed a marked tendency to delaminate upon electrolytic conditions at potentials above - 0.50V *vs* RHE. Work is currently underway to develop methods that impede the copper oxide films from delaminating prematurely.

Conflicts of interest

There are no conflicts to declare

Acknowledgements

The international Chair INTERMAT of E.P. has received funding from E2S UPPA an ANR PIA4 project. F.V. and A.V. thank E2S UPPA for their fellowships.

Notes and references

1 C. Chen, J. F. Khosrowabadi Kotyk and S. W. Sheehan, *Chem*, 2018, **4**, 2571–2586.
2 S. A. Bonke, M. Wiechen, D. R. MacFarlane and L. Spiccia, *Energy Environ. Sci.*, 2015, **8**, 2791–2796.
3 C. Hepburn, E. Adlen, J. Beddington, E. A. Carter, S. Fuss, N. Mac Dowell, J. C. Minx, P. Smith and C. K. Williams, *Nature*, 2019, **575**, 87–97.
4 G. Centi and S. Perathoner, *ChemSusChem*, 2010, **3**, 195–208.
5 O. S. Bushuyev, P. De Luna, C. T. Dinh, L. Tao, G. Saur, J. van de Lagemaat, S. O. Kelley and E. H. Sargent, *Joule*, 2018, **2**, 825–832.
6 P. De Luna, C. Hahn, D. Higgins, S. A. Jaffer, T. F. Jaramillo and E. H. Sargent, *Science*, 2019, **364**, eaav3506.
7 W. A. Smith, T. Burdyny, D. A. Vermaas and H. Geerlings, *Joule*, 2019, **3**, 1822–1834.
8 E. Boutin and M. Robert, *Trends in Chemistry*, 2021, **3**, 359–372.
9 X. Wang, Z. Wang, F. P. García de Arquer, C.-T. Dinh, A. Ozden, Y. C. Li, D.-H. Nam, J. Li, Y.-S. Liu, J. Wicks, Z. Chen, M. Chi, B. Chen, Y. Wang, J. Tam, J. Y. Howe, A. Proppe, P. Todorović, F. Li, T.-T. Zhuang, C. M. Gabardo, A. R. Kirmani, C. McCallum, S.-F. Hung, Y. Lum, M. Luo, Y. Min, A. Xu, C. P. O'Brien, B. Stephen, B. Sun, A. H. Ip, L. J. Richter, S. O. Kelley, D. Sinton and E. H. Sargent, *Nat Energy*, 2020, **5**, 478–486.

10 Y. Wang, Z. Wang, C.-T. Dinh, J. Li, A. Ozden, M. Golam Kibria, A. Seifitokaldani, C.-S. Tan, C. M. Gabardo, M. Luo, H. Zhou, F. Li, Y. Lum, C. McCallum, Y. Xu, M. Liu, A. Proppe, A. Johnston, P. Todorovic, T.-T. Zhuang, D. Sinton, S. O. Kelley and E. H. Sargent, *Nat Catal*, 2020, **3**, 98–106.
11 F. P. García de Arquer, C.-T. Dinh, A. Ozden, J. Wicks, C. McCallum, A. R. Kirmani, D.-H. Nam, C. Gabardo, A. Seifitokaldani, X. Wang, Y. C. Li, F. Li, J. Edwards, L. J. Richter, S. J. Thorpe, D. Sinton and E. H. Sargent, *Science*, 2020, **367**, 661–666.
12 C.-T. Dinh, T. Burdyny, M. G. Kibria, A. Seifitokaldani, C. M. Gabardo, F. P. García de Arquer, A. Kiani, J. P. Edwards, P. De Luna, O. S. Bushuyev, C. Zou, R. Quintero-Bermudez, Y. Pang, D. Sinton and E. H. Sargent, *Science*, 2018, **360**, 783–787.
13 A. Sedighian Rasouli, X. Wang, J. Wicks, G. Lee, T. Peng, F. Li, C. McCallum, C.-T. Dinh, A. H. Ip, D. Sinton and E. H. Sargent, *ACS Sustainable Chem. Eng.*, 2020, **8**, 14668–14673.
14 C. M. Gabardo, C. P. O'Brien, J. P. Edwards, C. McCallum, Y. Xu, C.-T. Dinh, J. Li, E. H. Sargent and D. Sinton, *Joule*, 2019, **3**, 2777–2791.
15 J. Li, A. Xu, F. Li, Z. Wang, C. Zou, C. M. Gabardo, Y. Wang, A. Ozden, Y. Xu, D.-H. Nam, Y. Lum, J. Wicks, B. Chen, Z. Wang, J. Chen, Y. Wen, T. Zhuang, M. Luo, X. Du, T.-K. Sham, B. Zhang, E. H. Sargent and D. Sinton, *Nat Commun*, 2020, **11**, 3685.
16 M. Luo, Z. Wang, Y. C. Li, J. Li, F. Li, Y. Lum, D.-H. Nam, B. Chen, J. Wicks, A. Xu, T. Zhuang, W. R. Leow, X. Wang, C.-T. Dinh, Y. Wang, Y. Wang, D. Sinton and E. H. Sargent, *Nat Commun*, 2019, **10**, 5814.
17 M. Gattrell, N. Gupta and A. Co, *Journal of Electroanalytical Chemistry*, 2006, **594**, 1–19.
18 R. Buonsanti, *Nat Catal*, 2021, **4**, 736–737.
19 J. Huang and R. Buonsanti, *Chem. Mater.*, 2019, **31**, 13–25.
20 P. Iyengar, M. J. Kolb, J. R. Pankhurst, F. Calle-Vallejo and R. Buonsanti, *ACS Catal.*, 2021, **11**, 4456–4463.
21 G. L. De Gregorio, T. Burdyny, A. Loiudice, P. Iyengar, W. A. Smith and R. Buonsanti, *ACS Catal.*, 2020, **10**, 4854–4862.
22 P. Iyengar, J. Huang, G. L. De Gregorio, C. Gadiyar and R. Buonsanti, *Chem. Commun.*, 2019, **55**, 8796–8799.
23 A. Loiudice, P. Lobaccaro, E. A. Kamali, T. Thao, B. H. Huang, J. W. Ager and R. Buonsanti, *Angew. Chem. Int. Ed.*, 2016, **55**, 5789–5792.
24 Y. Lu, H. Cao, S. Xu, C. Jia and G. Zheng, *RSC Adv.*, 2021, **11**, 21805–21812.
25 D. Ren, J. Gao, L. Pan, Z. Wang, J. Luo, S. M. Zakeeruddin, A. Hagfeldt and M. Grätzel, *Angew. Chem. Int. Ed.*, 2019, **58**, 15036–15040.
26 P. Seeharaj, N. Vittayakorn, J. Morris and P. Kim-Lohsoontorn, *Nanotechnology*, 2021, **32**, 375707.
27 H. Guzmán, D. Roldán, A. Sacco, M. Castellino, M. Fontana, N. Russo and S. Hernández, *Nanomaterials*, 2021, **11**, 3052.
28 S. Dongare, N. Singh, H. Bhunia and P. K. Bajpai, *Electrochimica Acta*, 2021, **392**, 138988.
29 C. Chen, X. Yan, S. Liu, Y. Wu, Q. Wan, X. Sun, Q. Zhu, H. Liu, J. Ma, L. Zheng, H. Wu and B. Han, *Angew. Chem. Int. Ed.*, 2020, **59**, 16459–16464.
30 Z. Pan, E. Han, J. Zheng, J. Lu, X. Wang, Y. Yin, G. I. N. Waterhouse, X. Wang and P. Li, *Nano-Micro Lett.*, 2020, **12**, 18.
31 G. Avgouropoulos, T. Ioannides and H. Matralis, *Applied Catalysis B: Environmental*, 2005, **56**, 87–93.
32 X. Wang, K. Klingan, M. Klingenhof, T. Möller, J. Ferreira de Araújo, I. Martens, A. Bagger, S. Jiang, J. Rossmeisl, H. Dau and P. Strasser, *Nature Communications*, 2021, **12**, 794.
33 J. Yuan and Y. Wang, *J. Electrochem. Soc.*, 2017, **164**, E475–E479.
34 M. Ma, K. Djanashvili and W. A. Smith, *Phys. Chem. Chem. Phys.*, 2015, **17**, 20861–20867.
35 M. Schreier, F. Héroguel, L. Steier, S. Ahmad, J. S. Luterbacher, M. T. Mayer, J. Luo and M. Grätzel, *Nat Energy*, 2017, **2**, 17087.
36 P. Li, J. Xu, H. Jing, C. Wu, H. Peng, J. Lu and H. Yin, *Applied Catalysis B: Environmental*, 2014, **156–157**, 134–140.
37 M. Le, M. Ren, Z. Zhang, P. T. Sprunger, R. L. Kurtz and J. C. Flake, *J. Electrochem. Soc.*, 2011, **158**, E45.
38 L. Mandal, K. R. Yang, M. R. Motapothula, D. Ren, P. Lobaccaro, A. Patra, M. Sherburne, V. S. Batista, B. S. Yeo, J. W. Ager, J. Martin and T. Venkatesan, *ACS Appl. Mater. Interfaces*, 2018, **10**, 8574–8584.
39 Department of Environmental Science and Engineering, Beijing University of Chemical Technology, Beijing 100029, P. R. China and J. Yuan, *Int. J. Electrochem. Sci.*, 2017, 8288–8294.
40 L. Yu, G. Li, X. Zhang, X. Ba, G. Shi, Y. Li, P. K. Wong, J. C. Yu and Y. Yu, *ACS Catal.*, 2016, **6**, 6444–6454.

41 A. P. Periasamy, R. Ravindranath, S. M. Senthil Kumar, W.-P. Wu, T.-R. Jian and H.-T. Chang, *Nanoscale*, 2018, **10**, 11869–11880.
42 T. N. Huan, D. A. Dalla Corte, S. Lamaison, D. Karapinar, L. Lutz, N. Menguy, M. Foldyna, S.-H. Turren-Cruz, A. Hagfeldt, F. Bella, M. Fontecave and V. Mougel, *Proc Natl Acad Sci USA*, 2019, **116**, 9735–9740.
43 J.-Y. Li, L. Yuan, S.-H. Li, Z.-R. Tang and Y.-J. Xu, *J. Mater. Chem. A*, 2019, **7**, 8676–8689.
44 K. C. Christoforidis and P. Fornasiero, *ChemCatChem*, 2019, **11**, 368–382.
45 L. Shang, X. Lv, H. Shen, Z. Shao and G. Zheng, *Journal of Colloid and Interface Science*, 2019, **552**, 426–431.
46 H.-Y. Kang, D.-H. Nam, K. D. Yang, W. Joo, H. Kwak, H.-H. Kim, S.-H. Hong, K. T. Nam and Y.-C. Joo, *ACS Nano*, 2018, **12**, 8187–8196.
47 F. Gao, X.-J. Liu, J.-S. Zhang, M.-Z. Song and N. Li, *Journal of Applied Physics*, 2012, **111**, 084507.
48 X. Xu, M. Zhang, J. Feng and M. Zhang, *Materials Letters*, 2008, **62**, 2787–2790.
49 Y. S. Lee, D. Chua, R. E. Brandt, S. C. Siah, J. V. Li, J. P. Mailoa, S. W. Lee, R. G. Gordon and T. Buonassisi, *Adv. Mater.*, 2014, **26**, 4704–4710.
50 A. M. Asiri, J. Gao, S. B. Khan, K. A. Alamry, H. M. Marwani, M. S. J. Khan, W. A. Adeosun, S. M. Zakeeruddin, D. Ren and M. Grätzel, *J. Phys. Chem. Lett.*, 2022, **13**, 345–351.
51 Y. Yang, D. Xu, Q. Wu and P. Diao, *Sci Rep*, 2016, **6**, 35158.
52 M. E. Aguirre, R. Zhou, A. J. Eugene, M. I. Guzman and M. A. Grela, *Applied Catalysis B: Environmental*, 2017, **217**, 485–493.
53 H.-J. Yang, H. Yang, Y.-H. Hong, P.-Y. Zhang, T. Wang, L.-N. Chen, F.-Y. Zhang, Q.-H. Wu, N. Tian, Z.-Y. Zhou and S.-G. Sun, *ChemSusChem*, 2018, **11**, 881–887.
54 S. C. Ray, *Solar Energy Materials*.
55 E. H. Dias, G. T. S. T. Da Silva, J. C. Da Cruz and C. Ribeiro, *ChemElectroChem*, , DOI:10.1002/celc.202200206.
56 H. Guzmán, D. Roldán, A. Sacco, M. Castellino, M. Fontana, N. Russo and S. Hernández, *Nanomaterials*, 2021, **11**, 3052.
57 Y. Lu, H. Cao, S. Xu, W. Feng, G. Hou, Y. Tang, H. Zhang and G. Zheng, *Journal of Colloid and Interface Science*, 2021, **599**, 497–506.
58 T. Kosugi and S. Kaneko, *J American Ceramic Society*, 1998, **81**, 3117–3124.
59 M. Pavan, S. Rühle, A. Ginsburg, D. A. Keller, H.-N. Barad, P. M. Sberna, D. Nunes, R. Martins, A. Y. Anderson, A. Zaban and E. Fortunato, *Solar Energy Materials and Solar Cells*, 2015, **132**, 549–556.
60 Y. S. Lee, J. Heo, M. T. Winkler, S. C. Siah, S. B. Kim, R. G. Gordon and T. Buonassisi, *J. Mater. Chem. A*, 2013, **1**, 15416.
61 F. Ye, J.-J. Zeng, X.-M. Cai, X.-Q. Su, B. Wang, H. Wang, V. A. L. Roy, X.-Q. Tian, J.-W. Li, D.-P. Zhang, P. Fan and J. Zhang, *Journal of Alloys and Compounds*, 2017, **721**, 64–69.
62 H. Tanaka, T. Shimakawa, T. Miyata, H. Sato and T. Minami, *Thin Solid Films*, 2004, **469–470**, 80–85.
63 M. T. S. Nair, L. Guerrero, O. L. Arenas and P. K. Nair, *Applied Surface Science*, 1999, **150**, 143–151.